Detector response artefacts in spectral reconstruction

Olsen, Ulrik Lund; Christensen, Erik D.; Khalil, Mohamad; Gu, Yun; Kehres, Jan

Published in:
Proc. SPIE 10391, Developments in X-Ray Tomography XI

Link to article, DOI:
10.1117/12.2272564

Publication date:
2017

Document Version
Publisher's PDF, also known as Version of record

PROCEEDINGS OF SPIE

SPIEDigitalLibrary.org/conference-proceedings-of-spie

Detector response artefacts in spectral reconstruction

Ulrik L. Olsen, Erik D. Christensen, Mohamad Khalil, Yun Gu, Jan Kehres

Ulrik L. Olsen, Erik D. Christensen, Mohamad Khalil, Yun Gu, Jan Kehres, "Detector response artefacts in spectral reconstruction," Proc. SPIE 10391, Developments in X-Ray Tomography XI, 103910Q (25 September 2017); doi: 10.1117/12.2272564

SPIE.

Event: SPIE Optical Engineering + Applications, 2017, San Diego, California, United States

Detector response artefacts in spectral reconstruction

Ulrik L. Olsen[a], Erik D. Christensen[b], Mohamad Khalil[a], Yun Gu[a], and Jan Kehres[a]

[a]Department of Physics, Technical University of Denmark, Fysikvej 2800, Lyngby, Denmark
[b]Niels Bohr Institute, University of Copenhagen, Universitetsparken 5, 2100, Copenhagen, Denmark

ABSTRACT

Energy resolved detectors are gaining traction as a tool to achieve better material contrast. K-edge imaging and tomography is an example of a method with high potential that has evolved on the capabilities of photon counting energy dispersive detectors. Border security is also beginning to see instruments taking advantage of energy resolved detectors. The progress of the field is halted by the limitations of the detectors. The limitations include nonlinear response for both x-ray intensity and x-ray spectrum. In this work we investigate how the physical interactions in the energy dispersive detectors affect the quality of the reconstruction and how corrections restore the quality. We have modeled detector responses for the primary detrimental effects occurring in the detector; escape peaks, charge sharing/loss and pileup. The effect of the change in the measured spectra is evaluated based on the artefacts occurring in the reconstructed images. We also evaluate the effect of a correction algorithm for reducing these artefacts on experimental data acquired with a setup using Multix ME-100 V-2 line detector modules. The artefacts were seen to introduce 20% deviation in the reconstructed attenuation coefficient for the uncorrected detector. We performed tomography experiments on samples with various materials interesting for security applications and found the structural similarity index to increase $> 5\%$ below 60 keV. Our work shows that effective corrections schemes are necessary for the accurate material classification in security application promised by the advent of high flux detectors for spectral tomography.

Keywords: Material classification, Energy resolving detectors, NDT, Spectral Tomography

1. INTRODUCTION

Attacks on the aviation infrastructure since the beginning of the millennium has caused large changes in the airport industry. In the US alone the 9/11 incident meant a 3-fold increase in the number of people employed for screening luggage and passengers.[1] Since the transatlantic plot august 9th 2006[2] the EU has enforced a ban on all European airports requiring travelers to remove all liquids, aerosols and gases (LAG's) from the baggage and limited the amounts to a maximum quanta of 100ml confined in a 1 liter transparent plastic bag. Subsequently the increased screening time required for each passenger has led to onerous waiting times at the security check-in and increased cost for scanners and personnel that has trickled from the airport to the airlines to the passengers.[3]

A C2 certification from the European Civil Aviation Conference (ECAC) allows screening of luggage containing laptops and large electronics. The C3 certification additionally allows the luggage to contain LAG's, both new levels of certification will help to alleviate some of the required divesting for passengers. While ECAC's C2 certifications have been given to scanners with fixed sources and detectors the C3 certification is yet to be awarded[4] and it is expected that only CT scanners with either rotating gantry or multi source instruments will pass initially. Reconstruction of the luggage to a 3D model is thus considered the holy grail of future aviation security. This may be true but leads to a significant number of challenges as experienced by medical CT.[5] Multi-Energy (ME) detection alleviates many of these problems[6] and the development of an efficient model for spectral CT would be able to address the primary airport security issue of fast detection of explosives with low false alarm rates.[7,8] As such the ME X-ray detectors represent a new paradigm in airport security scanning devices. The use of these energy dispersive technology provides X-ray images with a higher information content

Further author information:
Ulrik L. Olsen.: E-mail: ullu@dtu.dk, Telephone: +45 24 65 51 69

Developments in X-Ray Tomography XI, edited by Bert Müller, Ge Wang, Proc. of SPIE Vol. 10391,
103910Q · © 2017 SPIE · CCC code: 0277-786X/17/$18 · doi: 10.1117/12.2272564

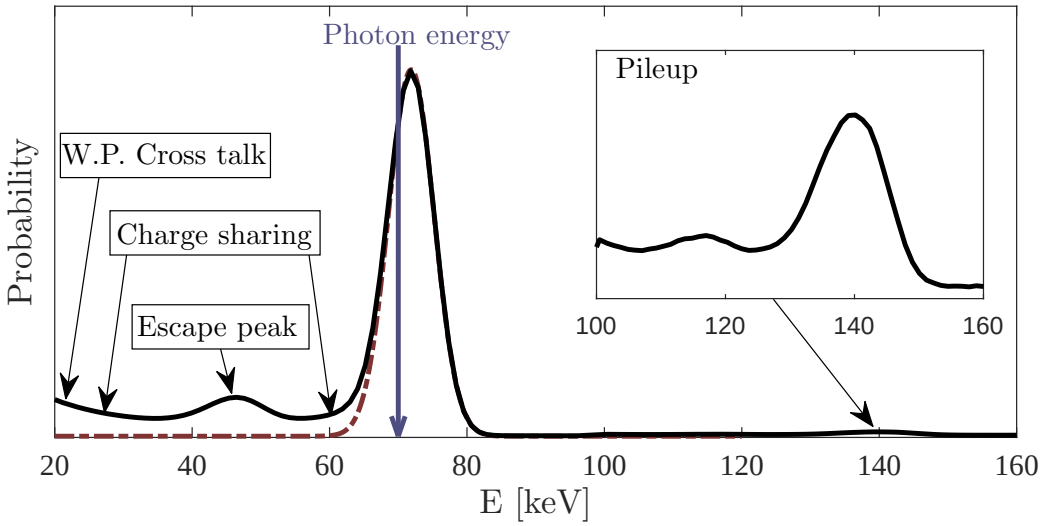

Figure 1. Spectrum measured with a Multix ME100 v2 detector at a monochromatic synchrotron irradiation of 70 keV. The spectrum shows the 4 primary distortion effect of the detector response: Weighing potential crosstalk, Charge sharing and Escape peaks. The zoom-in on the high energy spectrum in the "Pileup box" shows the pileup peak at 140 keV corresponding to to twice the energy of the incident peak. The dashed red line shows the ideal response using a finite energy resolution corresponding to the ME100 detector.

than conventional dual-energy detectors.[9] ME detectors greatly enhance the performance of tomographic techniques, and provide operators with significantly improved images leading to improved materials discrimination and reduced false alarms.

However, ME detectors, especially those with a fast readout, also stain the measured signal with a number of artefacts and in this work we investigate how the artefacts in turn influence the reconstruction and propose correction routines,[10] that successfully eliminates these artifacts both in the measured signal and in the reconstruction. The findings is also applicable outside of the security such as medical[11] and food quality assurance.[12]

Pixelated spectral detectors are predominantly made from CdTe absorber crystals.[13–15] Although some artefacts are general for photons counting detector the work here focuses on CdTe performance. A full description of the physical interaction can be found elsewhere[16–19] and we will here only reiterate the spectral distortions seen in fig. 1 caused by how the physical mechanism of detection occur in the detector. Here the four influences are listed in the order they are encountered in the spectrum:

- Weighing Potential (W.P.): This effect comes from the charges moving through the crystal drawn by the electrical field produced by the bias voltage. In the vicinity of another pixel the charge as in a capacitor induce a mirror charge in the neighbor pixel which is in some cases registered as a photon. The energy of the induced photon will mostly be at the very low end of the spectra which thus have a peak.

- Charge sharing: The incoming photon generates a charge cloud upon absorption. The size of the cloud is energy dependent. The more energy that is deposited in the crystal at the same time the more expulsion will the charge see corresponding to a fast initial increase in size. The charge is drawn into the charge collecting electrode by the applied bias field on the crystal. For charge close to the boundary between 2 or more pixel the charge can be split according the strength of the voltage field on both pixels with a corresponding decrease in perceived energy by either of the pixels. The effect draws the whole spectrum downwards but the cumulative effect of smaller charges being separated means that the lower end of the spectrum is increased.

- Fluorescence: this phenomenon describes how energy is lost from the pixel when an incoming X-ray excites the inner shell of the crystal atoms and a fluorescence photon is generated. For CdTe only K-shell fluorescence have sufficient energy to escape the pixel either entirely out of the detector or into a neighbor

pixel. For CdTe K-shell fluorescence photons can have 4 discrete energies from 25 keV to 31 keV. Since the fluorescence escapes easier from the surface of the crystal and incoming photons of lower energies are typically absorbed close the the surface of the crystal, this effect has an energy dependence. The effect is seen as a smaller signal 25-31 keV below the energy of the incoming photon.

- Pileup: Opposed to the other effects pile-up adds energy to the true value of the incoming photon. In this paper we deal with detectors operating in flux densities up to $5x10^6$ photons/mm^2/s, this means a very low detection time for the single photon in the order of hundreds of nano-seconds. Since the incoming flux has a statistical variation in time, pile-up occur even if the average time between photons is above this detection time. The effect of pile-up is a registered peak at the energy of the sum of the energies of the involves photons. This effect depends on the shape of the whole spectra and the incident flux is thus not the same for the flat field spectrum and the spectrum filtered by a sample.

Collectively these effects are the detector response and for the flux independent effect they can be described as a matrix (a detector response matrix (DRM)) which transforms the incident spectrum into the measured spectrum. It is obvious that the attenuation coefficient of a material change because of the detector response. This in turn influence the classification of explosives which is based on the signature of the attenuation coefficient. However another more subtle change occurs when the acquired data is used for spectral reconstructions. In spectral reconstruction the basic reconstruction method is to reconstruct each energy channel by itself. But in the case of spectral distortion the reconstruction algorithm is effectively experiencing that photons are appearing or disappearing in the projections. As opposed to the absorption efficiency which affect each energy bin independently the above described effects transfer photons or energy between the energy bins in a inter-spectral reshuffling.

Besides the influence of the detector the reconstruction quality is influenced by noise photon starvation and geometric misalignment. This work focuses on the detector response. We have divided the investigation into two parts first based on experimental data comparing the intensity levels between the raw detector signal and the radiograms corrected for detector response. Secondly the experimental data is used to generate virtual radiograms for all projections using the forward model of the reconstruction algorithm. One dataset resembles the response from an ideal detector while the other dataset has been convoluted with the DRM. The comparison is based on the reconstruction of these datasets. The use of virtual data removes the effect of noise, scatter from sample and environment and discrepancies between instrument and the geometry specified in the reconstruction algorithm.

The analysis of DRM for spectrally resolving detectors exist widely in literature[20–23] however not so much for methods to correct experimentally acquired data, and to the best of our knowledge the effect of DRM on spectral reconstruction have not been examined.

2. METHODOLOGY

2.1 Multispectral X-ray setup

All X-ray data are acquired at a general-purpose setup for spectral imaging built at the Technical University of Denmark (DTU) and presented in the work of Kehres *et al.*[24] In the order of beam propagation, the setup consists of an micro focus X-ray generator with height (z) movement; a primary slit; a sample stage featuring x, y, z and rotation movement; a secondary detector slit and a 1D detector on a detector stage with x, y, z movements. The generator is a Hamamatsu ML12161-07 operated at 150 kVp and 0.5 mA. The primary slit, positioned 246 mm from the focal spot, is a JJ X-ray IB-50-Air aligned for a fan beam with 0.6 mm beam height and 30 mm beam width at the slit position. The sample is positioned 500 mm from the source and the detector is 510 mm farther from the sample. The secondary slit is custommade from 5mm Tungsten blades placed 10 mm in front of the detector window with an opening of 0.6 mm, which is slightly less than the pixel size of 0.8 mm. The detector consists of two tiled modules of Multix Me-100 V2 using an 3 mm thick CdTe detector crystal. Each module has 128 pixels and separates the photons in 128 energy bins in the range 20 keV to 160 keV. Energy resolution of the detector is ≈7 keV FWHM evaluated at 70 keV.

To acquire one tomographic slice, the sample is rotated and imaged at 361 angular positions evenly spaced over 360°. At each position, the sample projection is acquired 100 consecutive times each with a 100 ms exposure

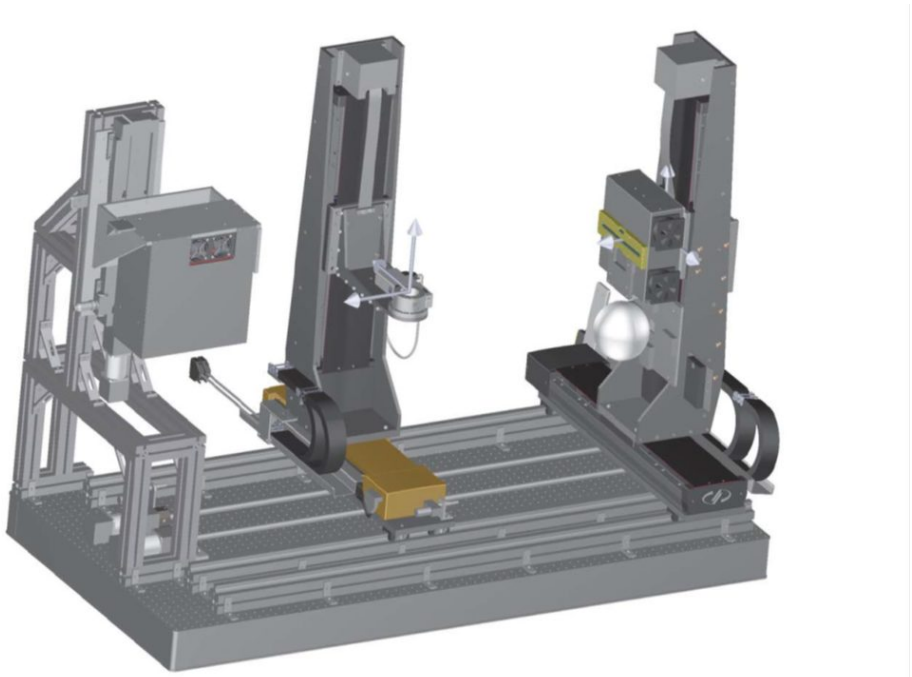

Figure 2. The general purpose instrument RB-150 at Department of Physics, DTU. From left to right the sketch shows the source on a height adjustable stage mounted with a slit adjustable in both directions up to a 50 mm opening, the sample stage with x,y,z movement all movements with speeds up to 200 mm/s. The sample stage is furthermore equipped with a rotation stage for tomographic scans. The detector stage has x, y and z movements and are prepared for various detector configuration up to a maximum of 8 Kg.

time. For each projection, the median value of each bin in each pixel is computed from the set of 100 equivalent acquisition. The detector response is corrected using a method developed by Christensen *et al*[10] for spectral CT applications. The flat field measurement is performed subsequently in the same setup but with the sample removed.

For our experiments, we created a physical phantom (Fig. 3(a)) of four glass bottles containing four different materials with very similar attenuation coefficients. The materials are water (H_2O), 30 wt% hydrogen peroxide (H_2O_2), ethanol (C_2H_5OH) and PETN ($C_5H_8N_4O_{12}$)*. The materials were placed in glass bottles. To provide a significant change in the transmitted spectra for the different projections, sheets of materials, with a heavy attenuation relative to the 4 materials, were placed on two sides of the collection of glass bottles. The sheets were 2 mm of aluminum and 4 mm of PVC. PVC contains lead which leads to a shift in the absorption at the K-edge energy as seen in the attenuation coefficient in fig. 4(a). This collection of items we enclosed in a cylinder of PMMA to keep their position during the rotation of the scan.

2.2 Virtual dataset

The experimental dataset has limitation from finite noise levels and finite resolution of geometry accuracy. Contributions from scattered radiation both from the sample and the environment can also cause effects in the reconstruction similar to those from detector response.[25–27] Hence we manufactured a virtual dataset built on experimental data that allowed us to focus on the spectral differences between corrected and uncorrected projections. We used the reconstruction of energy bin 60 corresponding to 85 keV. This energy bin only has a small influence from the corrections algorithms. The reconstructed slice was manually segmented into each of the 8 different materials. These segments were defined as the position of the material in the virtual phantom. For each of the analyzed energy bins the corresponding attenuation coefficient was found for each of the materials.

*X-ray correct simulant from Renful Premier Technologies

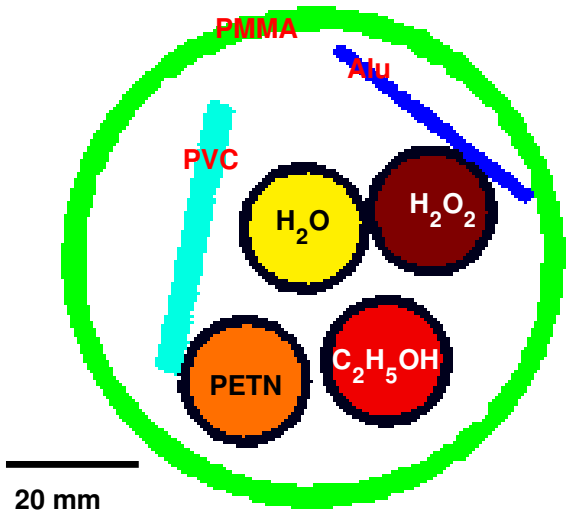

Figure 3. The virtual phantom used in the experiments, consisting of 4 glass bottles of material (water, 30 $wt\%$ hydrogen peroxide, PETN and ethanol). To make the collected spectra vary between projections, sheets of relatively heavy attenuation (4 mm PVC and 2 mm aluminum) were inserted next to the bottles. Finally the phantom was enclosed in a PMMA cylinder to keep items from shifting during the scan.The schematic shows the position of the components in the phantom. The schematic is based on a manual segmentation of a reconstruction.

The attenuation coefficient for each material was found from the corresponding area in the reconstruction of the experimental data. The attenuation was taken from the experimental data that had been spectrally corrected. Subsequently for each energy bin the virtual projections was found from the generated phantom using the forward model in the reconstruction algorithm.

To produce the ideal reconstruction the projections was not further processed before the reconstruction,this corresponds to having a fully corrected detector response. For the raw reconstruction the projections were applied the DRM for charge sharing, escape peaks and weighing potential, this corresponds to the uncorrected response from a detector with artefacts. The pile-up effect was not used to avoid having to include source power as parameters in the analysis. Finally the two datasets was produced by reconstructing the virtual projections.

2.3 Reconstruction method

The motivation for our work is the development of a fixed gantry security scanner. The requirements for a compact size dictates both few projections but also that the views from source-detectors pairs are non-uniformly distributed around the sample. Since we are analyzing the effect of spectral corrections on the reconstruction we need a reconstruction method which handles this type of projections. Using a typical filtered back projections algorithm would not give an adequate reconstruction quality. Iterative methods such as Algebraic Reconstruction Technique (ART) have been shown to handle few projections well, but comparing the influence for different algorithms is outside the scope of this work. In literature many descriptions of spectral reconstruction methods are found[28,29] but as a rule they assume perfectly sampled or intrinsically corrected data[30] or at the most data affected by statistical noise.[31] This provide us no information of the best suited algorithm and instead we have used a well-known ART algorithm developed by Sidky *et al.*[32] It uses Total Variation (TV) for regularization which will limit the noise from reconstructing data from narrow energy bins, although the regularization can also remove some artefacts from the spectral manipulation. The effect of regularization will not be investigated at this time and we will use the same parameters for all reconstructions. We used 500 iteration of ART each with 10 iteration of TV. The relaxation parameter was 0.8 and 0.3 for ART and TV respectively.

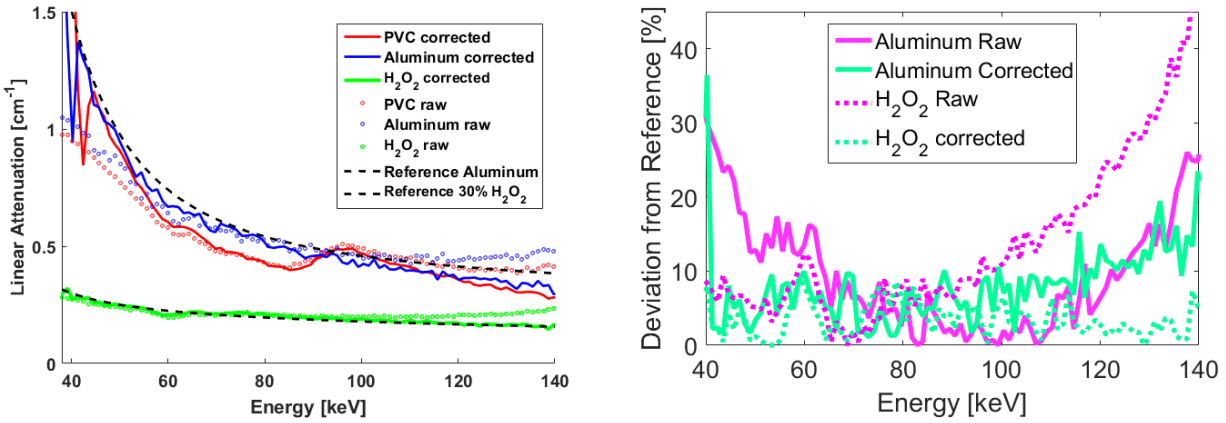

(a) (b)

Figure 4. (a) The experimentally measured attenuation coefficients of selected materials from the phantom. We have focused on the energy range 40-140 keV. Reference data from NIST[33] is shown for reference for aluminum and hydrogen peroxide. (b) The absolute deviation from two reference material aluminum (solid lines) and H_2O_2 (dashed lines). The reconstructed value from unprocessed raw projections in magenta and the values from corrected projections are shown in cyan. The deviation is found from the ratio between the absolute deviation and the reference spectra.

3. RESULTS AND DISCUSSION

3.1 Reconstructed intensity

The obvious question is how the attenuation of the reconstructed materials resemble reference data. The long exposures used for the data allowed a reasonable Signal to Noise Ratio (SNR) for most energy bins unless the attenuation of the sample quenched the photon count too much. In the entirety of this work we have considered each energy bin separately without binning. Although the energy resolution of the detector merits a far lower number of bins the correction algorithms works on the full range of energy bins since the corrections have effects from the discrete k-shell activation that merits a high energy resolution. In this section we do not use the virtual datasets described above.

In fig. 4 the correspondence between reconstructions and reference data provide by NIST[33] is shown. The data set contains data from 128 bins covering the range from 20 keV to 160 keV but here the bins below 40 keV is excluded since photon starvation make these data noisy, similarly the source emission is only significant below 140 keV and the spectra is cut above that. The graph compares a reconstruction based on the raw projections and a reconstruction based on the same projections but corrected for the detector response. The corrections are done on spectra of photon counts but here consistently shown for the calculated attenuation spectra. From the reconstructions the attenuation is found for H_2O_2 and aluminum. The attenuation is found from the median intensity in the areas of the material as it is presented in the reference phantom. From the attenuation graph (a) the effect of charge sharing is seen for the low energy range of the uncorrected reconstruction. charge sharing push energy to lower energies which makes the properties of the lower energies resemble that of the higher energies. Thus the low energy attenuation is lowered since the attenuation at higher energies are lower. Similarly the pileup effect pushes photons to the higher energy bins. Since the lower energies have a higher attenuation the attenuation at higher energies are measured as higher. Furthermore the pileup effect is flux dependent, which means that the pileup effect is lower when the sample is in the beam to block photons from hitting the detector. The decrease in pileup photons when the sample is in the beam further increases the measured attenuation coefficient. The central range of energies have a higher number of photons than both the high and low range of energies even if photons are shifted to and from this energy range the effect on the measurement is smaller.

The relative attenuation deviation is shown in fig. 4 (b) for the same two materials. For the higher attenuating aluminum the attenuation coefficient is decreased 15-30 % below 60 keV for the uncorrected spectrum for the higher energy range both the corrected and the raw spectra shows a deviation between 10 % and 20 %. The reference used is for pure aluminum however specifically at higher energies the attenuation are more sensitive

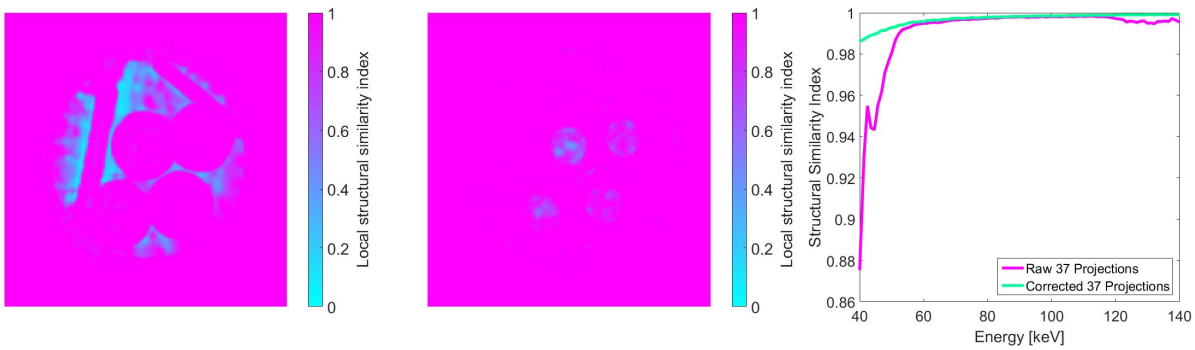

(a) (b) (c)

Figure 5. The structural similarity index (SSI) is found for each of the energy bins in the dataset. The values are found using the manually segmented phantom as reference. The intensities for the reference phantom was found from the simulated reconstruction using 361 projections. For the reference for the "raw" SSI data the projections had been applied the DRM for charge sharing, escape peaks and weighing potential. For the reference to the "corrected" SSI data the projections were left as simulated as the "ideal" response. (a) the SSI map of the "raw" data at 45 keV the dissimilarities are mostly found in the background (b) the SSI map of the "corrected" data at 45 keV here the dissimilarities are for the areas of the materials. (c) The curve for the global SSI for the entire spectra. At 45 keV the "raw" curve has an index of 95 % while the "corrected" dataset has an index of 99 %

.

to the specific stoichiometry of the aluminum, where contents of magnesium and zinc can drag the attenuation coefficient both up or down. The attenuation deviation curves for the material of 30 wt% H_2O_2 are below 10 % for both corrected and uncorrected spectra however at high energies the uncorrected attenuation rises above 40 % deviation. Compared to aluminum, H_2O_2 has a flatter attenuation curve and thus attenuate all parts of the spectra more uniformly, this means that the ratio of charge sharing, weighing potential cross talk and escape peaks are maintained. The flux density however is changed and this means that the flux dependent pileup is reduced. A reduced pileup effect translates into the higher attenuation at higher energies that we observe.

3.2 Reconstructed shape similarity

In the following the results are based on the virtual dataset described above. Beside the spectral accuracy the reconstruction can be evaluated with a full-reference approach incorporating both intensity and shape. The structural similarity index (SSI) is an image evaluation method which deal with the perceived accuracy.[34] The SSI was developed as an alternative to finding the mean squared error. The method was aimed at better evaluating how the Human Visual System (HSV) would perceive the quality of an image. This meant that contrast and intensity was evaluated locally rather than on an absolute global scale. The motivating application of this work is classification of specific materials (explosives). Whether these materials are recognized at their reference attenuation levels or through a calibrated instrument-specific signature is not significant for this application. If the SSI is the same for both uncorrected and raw reconstruction it could thus be interpreted that the materials could be segmented and classified equally well, however from customized material signatures.

The importance for this section is not the absolute accuracy of the attenuation curves. Rather the consistency with the material's provenance are significant. The reference for the SSI evaluation are thus not the NIST reference curves but the attenuation coefficient from the virtual phantom.

The measured structural similarity index in fig. 5(c) supports the findings from the comparison of attenuation curves in section 3.1. The lower energy range is negatively affected for the raw data while the middle range follows the corrected reconstructions. Since we have not included the pileup effect for the virtual datasets the upper energy range is similar to the reference for both reconstructions.

In fig. 5(a) and (b) the local distribution of the similarity index is shown for the energy bin corresponding to 45 keV. It shows how the dissimilarities for the uncorrected reconstruction are placed in the background. For the corrected reconstruction the much smaller dissimilarities stays in the areas where the materials exists in the

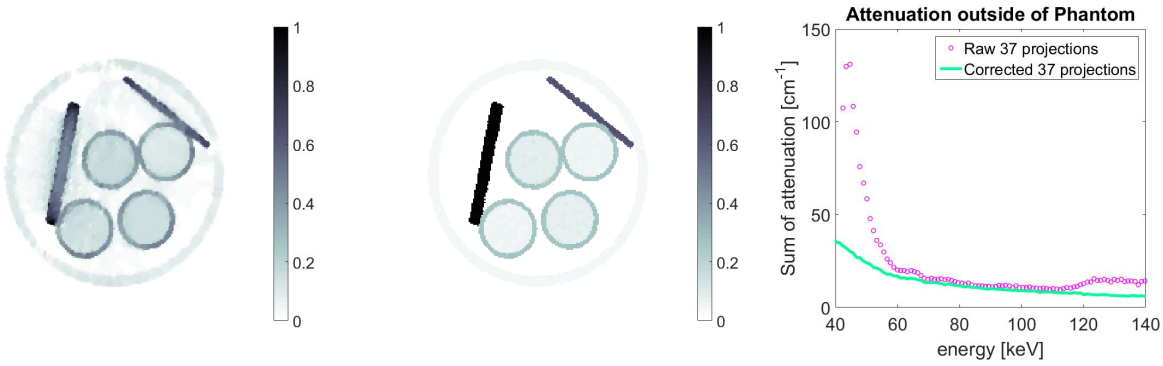

(a) (b) (c)

Figure 6. Attenuation maps from reconstructions using 37 projections. The maps show the attenuation at 36 keV. The intensity in the maps are normalized to better compare the background intensity. (a) The reconstruction from simulated raw projections a higher background attenuation at the level of 0.1 to 0.2 is visible inside the PMMA cylinder relative to (b) the reconstruction from the ideal projections. (c) Graph of the sum of the background attenuation for the range of energy bins. Below 60 keV the intensity for the uncorrected data increase significantly both in absolute terms and relative to the corrected data. The difference for the two datasets changes from being negligible between 60 keV and 120 keV to 200-300 % of the attenuation sum of the corrected data below 60 keV.

reference. This means that the uncorrected reconstruction will have a worse retention of shape compared to the corrected reconstruction.

Airport luggage constitutes a cluttered sample for which shape retention is important. To investigate this further we focused on the intensity in the background. First we had to consider the functionality of our reconstruction algorithm. The reconstruction algorithm automatically recognized Lines Of Response (LOR's) that only went through air and did not hit attenuating objects in the sample. The part of the reconstruction seen by these LOR's are forced to the background value which in this case is zero. Anything outside the PMMA cylinder is thus always zero for these number of projections. Any differences would hence be within the PMMA cylinder.

In fig. 6(a) and (b) the reconstruction from virtual raw or corrected projections respectively is shown. For the corrected reconstruction any background attenuation is not visible. The raw reconstruction has significant background attenuation especially close to the materials of heavier attenuation. The graph (c) showing the sum of all attenuation values in the background show that below 60 keV the raw reconstruction has 2-3 times the amount of misplaced attenuation compared to the corrected reconstruction. This factor is maintained throughout the range of lower energies even as the sum of misplaced attenuation also increases for the corrected reconstruction.

4. CONCLUSION

We have tested the influence of the detector response for radiographs used as projections for CT reconstructions. The results showed that the used correction method did indeed bring the attenuation coefficient close to reference values also after a reconstruction. We then developed a virtual model based on experimental data which allowed us to isolate the influence from noise, mis-calibration of geometry and scatter contribution from the findings. The data from the virtual model was used to evaluate the perceived difference, base on the difference of local relative contrast and intensity. The perceived difference was found to have the same correspondence as the absolute difference to the energy ranges where the spectral corrections were most severe. This means that even local contrast is affected by the detector response. We deduce from this that even a classification method customized for the raw detector response would experience a lack of consistency of attenuation signatures. the classification would thus be worse for the uncorrected detector signal.

A less intuitive finding is that the reconstructed shapes can be influenced by the reconstruction algorithm assigning attenuation to the background and possibly also to objects close to materials with relatively larger attenuation. This we also interpret to mean that the consistency in classification is reduced by any detector response, and that a good correction method must be employed.

ACKNOWLEDGMENTS

The authors acknowledges Innovation Fund Denmark for financing this work.

REFERENCES

[1] Blalock, G., Kadiyali, V., and Simon, D. H., "The impact of post-9/11 airport security measures on the demand for air travel," *The Journal of Law and Economics* **50**(4), 731–755 (2007).

[2] Seidenstat, P. and Splane, F. X., [*Protecting airline passengers in the age of terrorism*], ABC-CLIO (2009).

[3] Wandmaker, S., "Dirty water," *Aviation Security International* **3** (2017).

[4] ECAC, "Ecac-cep-edscb-web-update-6-june-2017." https://www.ecac-ceac.org/cep (Retrieved 06-07-2017).

[5] Barrett, J. F. and Keat, N., "Artifacts in ct: recognition and avoidance," *Radiographics* **24**(6), 1679–1691 (2004).

[6] Rajendran, K., Walsh, M., De Ruiter, N., Chernoglazov, A., Panta, R., Butler, A., Butler, P., Bell, S., Anderson, N., Woodfield, T., et al., "Reducing beam hardening effects and metal artefacts in spectral ct using medipix3rx," *Journal of Instrumentation* **9**(03), P03015 (2014).

[7] Wells, K. and Bradley, D., "A review of x-ray explosives detection techniques for checked baggage," *Applied Radiation and Isotopes* **70**(8), 1729–1746 (2012).

[8] Singh, S. and Singh, M., "Explosives detection systems (eds) for aviation security," *Signal Processing* **83**(1), 31–55 (2003).

[9] Gorecki, A., Brambilla, A., Moulin, V., Gaborieau, E., Radisson, P., and Verger, L., "Comparing performances of a CdTe X-ray spectroscopic detector and an X-ray dual-energy sandwich detector," *J. Instrum.* **8** (2013).

[10] Christensen, E. D., Gu, Y., Kehres, J., Feidenhans'l, R., and Olsen, U. L., "Spectral correction algorithm for multispectral cdte x-ray detectorsspectral correction algorithm for multispectral cdte x-ray detectors," in [*Proc. SPIE, Radiation Detectors in Medicine, Industry, and National Security XVIII (accepted)*], (2017).

[11] Taguchi, K., Srivastava, S., Kudo, H., and Barber, W. C., "Enabling photon counting clinical x-ray ct," in [*Nuclear Science Symposium Conference Record (NSS/MIC), 2009 IEEE*], 3581–3585, IEEE (2009).

[12] Einarsson, G., Jensen, J. N., Paulsen, R. R., Einarsdottir, H., Ersbøll, B. K., Dahl, A. B., and Christensen, L. B., "Foreign object detection in multispectral x-ray images of food items using sparse discriminant analysis," in [*Scandinavian Conference on Image Analysis*], 350–361, Springer (2017).

[13] Vavrik, D., Holik, M., Jakubek, J., Jakubek, M., Kraus, V., Krejci, F., Soukup, P., Turecek, D., Vacik, J., and Zemlicka, J., "Modular pixelated detector system with the spectroscopic capability and fast parallel read-out," *Journal of Instrumentation* **9**(06), C06006 (2014).

[14] Brambilla, A., Ouvrier-Buffet, P., Gonon, G., Rinkel, J., Moulin, V., Boudou, C., and Verger, L., "Fast cdte and cdznte semiconductor detector arrays for spectroscopic x-ray imaging," *IEEE Transactions on Nuclear Science* **60**(1), 408–415 (2013).

[15] Bellazzini, R., Spandre, G., Brez, A., Minuti, M., Pinchera, M., and Mozzo, P., "Chromatic x-ray imaging with a fine pitch cdte sensor coupled to a large area photon counting pixel asic," *Journal of Instrumentation* **8**(02), C02028 (2013).

[16] Redus, R. H., Pantazis, J. A., Pantazis, T. J., Huber, A. C., and Cross, B. J., "Characterization of CdTe detectors for quantitative X-ray spectroscopy," *IEEE Trans Nucl Sci* **56**, 2524–2532 (August 2009).

[17] Guerra, P., Santos, A., and Darambara, D. G., "Development of a simplified simulation model for performance characterization of a pixellated CdZnTe multimodality imaging system," *Phys. Med. Biol.* **53**, 1099–1113 (2008).

[18] Plagnard, J., "Comparison of measured and calculated spectra emitted by the X-ray tube used at the Gustave Roussy radiobiological service," *X-ray Spectrom.* **43**, 298–304 (2014).

[19] Knoll, G. F., [*Radiation Detection and Measurement*], John Wiley & sons, Inc., 3 ed. (1999).

[20] Fernandez, J. E., Scot, V., and Sabbatucci, L., "A modeling tool for detector resolution and incomplete charge collection," *X-ray Spectrom.* **44**, 177–182 (2015).

[21] Cammin, J., Xu, J., Barber, W. C., Iwanczyk, J. S., Hartsough, N. E., and Taguchi, K., "A cascaded model of spectral distortions due to spectral response effects and pulse pileup effects in a photon-counting X-ray detector for CT," *Med. Phys.* **41**(4) (2014).

[22] Cammin, J., Kappler, S., Weidinger, T., and Taguchi, K., "Evaluation of models of spectral distortions in photon-counting detectors for computed tomography," *J. Med. Imaging* **3**(023503) (2016).

[23] Roessl, E., Daerr, H., Engel, K. J., Thran, A., Schirra, C., and Proksa, R., "Combined effects of pulse pile-up and energy response in energy-resolved, photon-counting computed tomography," in [*Nuclear Science Symposium and Medical Imaging Conference (NSS/MIC), 2011 IEEE*], 2309–2313, IEEE (2011).

[24] Kehres, J., Lyksborg, M., and Olsen, U. L., "Threat detection of liquid explosives and precursors from their X-ray scattering pattern using energy dispersive detector technology," *Submitted to SPIE Optics and Photonics* (2017).

[25] Busi, M., Olsen, U. L., Knudsen, E. B., Frisvad, J. R., Kehres, J., Christensen, E. D., Khalil, M., and Haldrup, K., "A monte carlo simulation of scattering reduction in spectral x-ray computed tomography," in [*Proc. SPIE, Radiation Detectors in Medicine, Industry, and National Security XVIII (accepted)*], (2017).

[26] Wiegert, J., Engel, K. J., and Herrmann, C., "Impact of scattered radiation on spectral ct," in [*Proc. SPIE*], **7258**, 72583X (2009).

[27] Johns, P. C. and Yaffe, M., "Scattered radiation in fan beam imaging systems," *Medical physics* **9**(2), 231–239 (1982).

[28] Pan, X., Chen, B., Zhang, Z., Pearson, E., Sidky, E., and Han, X., "Optimization-based reconstruction exploiting spectral information in ct," in [*The Third International Conference on Image Formation in X-Ray Computed Tomography*], 228–232 (2014).

[29] Rigie, D. S. and La Riviere, P. J., "A generalized vectorial total-variation for spectral ct reconstruction," in [*Proceedings of the Third International Conference on Image Formation in X-ray Computed Tomography*], **1**(1), 9–12 (2014).

[30] Egan, C. K., Wilson, M. D., Veale, M. C., Seller, P., Jacques, S. D., and Cernik, R. J., "Material specific x-ray imaging using an energy-dispersive pixel detector," *Nuclear Instruments and Methods in Physics Research Section B: Beam Interactions with Materials and Atoms* **324**, 25–28 (2014).

[31] Rose, S., Andersen, M. S., Sidky, E. Y., and Pan, X., "Noise properties of ct images reconstructed by use of constrained total-variation, data-discrepancy minimization," *Medical physics* **42**(5), 2690–2698 (2015).

[32] Sidky, E. Y., Kao, C.-M., and Pan, X., "Accurate image reconstruction from few-views and limited-angle data in divergent-beam ct," *Journal of X-ray Science and Technology* **14**(2), 119–139 (2006).

[33] NIST, "X-ray form factor, attenuation, and scattering tables." http://physics.nist.gov/PhysRefData/FFast/html/form.html (Retrieved 08-06-2017).

[34] Wang, Z., Bovik, A. C., Sheikh, H. R., and Simoncelli, E. P., "Image quality assessment: from error visibility to structural similarity," *IEEE transactions on image processing* **13**(4), 600–612 (2004).